Solar Energy Materials & Solar Cells 231 (2021) 111297

Contents lists available at ScienceDirect

Solar Energy Materials and Solar Cells

journal homepage: www.elsevier.com/locate/solmat

Changes in hydrogen concentration and defect state density at the poly-Si/SiO_x/c-Si interface due to firing

Christina Hollemann [a,*], Nils Folchert [a], Steven P. Harvey [b], Paul Stradins [b], David L. Young [b], Caroline Lima Salles de Souza [c], Michael Rienäcker [a], Felix Haase [a], Rolf Brendel [a,e,f], Robby Peibst [a,d]

[a] Institut für Solarenergieforschung Hameln (ISFH), Am Ohrberg 1, D-31860, Emmerthal, Germany
[b] National Renewable Energy Laboratory Golden, CO, USA
[c] Colorado School of Mines, Golden, CO, USA
[d] Institute of Electronic Materials and Devices, Leibniz Universität Hannover, Schneiderberg 32, D-30167, Hannover, Germany
[e] Laboratory of Nano and Quantum Engineering, Leibniz Universität Hannover, Schneiderberg 39, D-30167, Hannover, Germany
[f] Institute for Solid State Physics, Leibniz Universität Hannover, Appelstraße 2, D-30167, Hannover, Germany

ARTICLE INFO

Keywords:
Passivating contacts
Hydrogen
POLO
MarcoPOLO
Modeling
Firing

ABSTRACT

We determined the density of defect states of poly-Si/SiO_x/c-Si junctions featuring a wet chemical interfacial oxide from lifetime measurements using the MarcoPOLO model to calculate recombination and contact resistance in poly-Si/SiO_x/c-Si-junctions. In samples that did not receive any hydrogen treatment, the $D_{it,cSi}$ is about 2 $\times$ 10^{12} cm^{-2} eV^{-1} before firing and rises to 3–7 $\times$ 10^{12} cm^{-2} eV^{-1} during firing at measured peak temperatures between 620 °C and 863 °C. To address the question of why AlO_x/SiN_y stacks in contrast to pure SiN_y layers for hydrogenation during firing provides better passivation quality, we have measured the hydrogen concentrations at the poly-Si/SiO_x/c-Si interface as a function of AlO_x layer thickness and compared these to J_0 and calculated $D_{it,c\text{-}Si}$ values. We observe an increase of the hydrogen concentration at the SiO_x/c-Si interface upon firing as a function of the firing temperature that exceeds the defect concentrations at the interface several times. However, the AlO_x layer thickness appears to cause an increase in hydrogen concentration at the SiO_x/c-Si interface in these samples rather than exhibiting a hydrogen blocking property.

1. Introduction

In recent years the application of passivating contacts consisting of a highly doped polycrystalline silicon (poly-Si) layer on a thin interfacial oxide (POLO) has gained strong interest. Their high efficiency potential has been demonstrated in lab-scale, with both-side contacted solar cells with a conversion efficiency of 26.0% [1] and an interdigitated back contacted cell that used POLO junctions for both polarities with a record conversion efficiency of 26.1% [2]. However, in the transfer of laboratory cells to industrial cells, which is now being pursued [3,4], it is necessary to integrate high-temperature firing processes to form the screen-printed contacts into the cell process. It has been shown that the firing process can negatively affect the passivation quality of the poly-Si structures both in the contacted and non-contacted regions [5–7]. Furthermore, it has also been found that hydrogen passivation is essential for the preparation of highly passivating poly-Si junctions, which applies especially for junctions that are fired [8,9]. For this purpose, hydrogen needs to be brought to the SiO_x/c-Si interface. This is often done via hydrogen-containing capping layers and subsequent annealing processes [10]. Therefore, hydrogen-rich a-Si:H, SiN_y, and AlO_x layers have established themselves as suitable hydrogen sources. The passivation quality can be significantly improved with these layers, both individually or as a stack (SiN_y, AlO_x or SiN_y/AlO_x and AlO_x/SiN_y/AlO_x) [8,9,11–19]. However, also detrimental results have been observed after firing [8,9,14,20]. In the recent paper by Hollemann et al. [20], we observed that when firing SiN_y/n-type poly-Si stacks above 760 °C, there is a significant increase in J_0, which was also seen by Kang et al. [8] before. In our case, this increase was in some cases accompanied by strong blistering of the entire poly-Si/SiN_y stack. All the samples with SiN_y capping had in common that the deterioration of J_0 was irreversible. However, samples fired without any capping layer could be improved again by annealing at 425 °C for 30 min. This indicated that

* Corresponding author.
E-mail address: c.hollemann@isfh.de (C. Hollemann).

https://doi.org/10.1016/j.solmat.2021.111297
Received 14 May 2021; Received in revised form 25 June 2021; Accepted 19 July 2021
Available online 29 July 2021

firing in the presence of hydrogen induces different defects than firing without hydrogen present.

However, using an AlO_x/SiN_y stack leads to a much lower increase in J_0 after firing [8,20]. Thus, the question arises, "what is the reason for this positive effect of an intermediate AlO_x layer"? A possible hint was given by Kang et al. [8], who showed that an AlO_x/SiN_y stack did not lead to an increased but to a lower concentration of hydrogen at the interface as compared to samples with SiN_y single layers. Based on this investigation that the J_0 value does not solely decrease with increasing hydrogen content at the interface and the observation of strong blistering, we have suggested that above a specific concentration, hydrogen has a negative effect on the passivation quality [20]. This is consistent with a general observation that excess hydrogen can cause defects (such as platelets [21]) in silicon by breaking Si–Si (and possibly Si–O–Si) bonds.

Furthermore, we assume that the AlO_x layer serves as a diffusion barrier, as suggested by Secondary Ion Mass Spectrometry (SIMS) measurements from Kang et al. [8] and shown by Helmich et al. [22] based on indirect investigations of the in-diffused hydrogen content into the c-Si bulk material. In this work, we investigate this hypothesis in more detail. Therefore, we study the surface passivation stability upon firing, without capping the poly-Si and with an AlO_x/SiN_y capping at various T_{firing}. For this purpose, we fire nPOLO samples with AlO_x/SiN_y stacks and varying AlO_x layer thickness at different temperatures and examine both the passivation quality in terms of defect state densities and J_0 and the hydrogen concentration at the SiO_x/c-Si interface by SIMS measurements.

2. Experimental

a. Sample Preparation

We prepare symmetric test samples as shown in Fig. 1 on p-type (boron-doped) Czochralski-grown, 20 Ω cm Si wafer material. First, all samples are etched in a KOH-based solution to remove the saw damage and are subsequently cleaned using an RCA cleaning sequence. We then – according to ellipsometry – grow a 1.5 ± 0.2 nm-thick oxide by a wet chemical process in de-ionized water with diluted ozone. Subsequently, we cap the oxide by a 220 nm-thick low-pressure chemical vapor deposited (LPCVD) in-situ n-type doped poly-Si layer. After the deposition, the samples are annealed during a wet oxidation process in a tube furnace for 30 min at 820 °C or 860 °C (different for the two batches shown in this work), followed by a subsequent 1-h process step at 550 °C. It has been reported that these annealing temperatures can lead to the formation of pinholes for oxides with thicknesses of 1.2 nm–2.5 nm [23,24]. We then remove the oxide grown on the poly-Si by 40% HF, leading to a poly-Si thickness of about 160 nm.

All samples are coated with atomic layer deposited (ALD) AlO_x layer coating of different thicknesses between 2 and 15 nm. Subsequently, a 100 nm-thick SiN_y layer with a refractive index of n = 2.05 is deposited in a microwave-assisted plasma-enhanced chemical vapor deposition (MA-PECVD) tool at a chamber temperature of 500 °C. The H_2 process gas is replaced by D_2 gas during SiN_y deposition, with the aim of incorporating deuterium into the SiN_y layer. Using deuterated SiN_y allows to separate hydrogen from different sources in SIMS and to take advantage of the much lower SIMS detection limit for deuterium [25]. The other process gases, ammonia (NH_3) and silane (SiH_4), are not replaced so that both hydrogen and deuterium are present in the SiN_y layer.

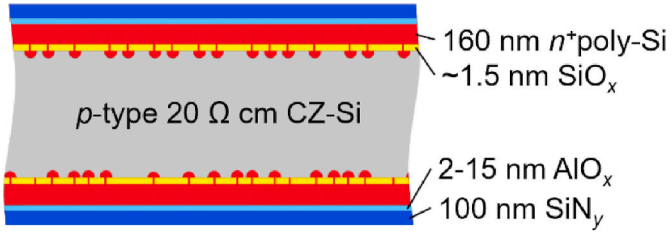

Fig. 1. Schematic illustration of the sample structure.

The subsequent firing takes place in an industrial infrared conveyor-belt furnace using a typical temperature profile (for details, see Ref. [20]) for the firing of metallization pastes using different peak temperatures, which range from 620 °C to 863 °C. The sample temperature profiles are monitored by a temperature probe pressed on a wafer and recorded using a DATAPAQ Insight Oven Tracker.

b. Measurement methods

The level of surface passivation is evaluated by quasi-steady-state photoconductance decay (QSSPC) measurements using a Sinton lifetime tester. The J_0 values are extracted using the method of Kane and Swanson [26] and the Auger parametrization of Richter et al. [27].

The doping profiles of the poly-Si are determined by electrochemical capacitance-voltage (ECV) profiling. The Time of Flight Secondary Ion Mass Spectrometry profiling (ToF-SIMS) is performed using an ION-TOF TOF-SIMS V spectrometer. A 30 KeV Bi + beam is utilized with a 1 pA pulsed beam current, and sputtering is completed with both 1 keV and 3 keV sputter gun energies, at 10 and 40 A beam current, respectively. The resulting profiles are quantified using implanted Si standards and thus do not apply to the SiN_y layers. The hydrogen content inside the SiN_y was determined using Fourier-transform infrared spectroscopy (FTIR) measurement. Therefore we determined the Si–N, Si–H, and N–H bond concentrations and thus the hydrogen concentration inside the SiN_y layer using calibration constants taken from Yin et al. [28].

c. Determination of maximum density of defect states

We determine the density of defect states from lifetime measurements using the MarcoPOLO model [29]. The MarcoPOLO model is a semi-analytic model that self-consistently solves the Poisson-equation in the poly-Si/SiO_x/c-Si structure to find the band-bending. In that model, the defect density $D_{it,cSi}$ at the SiO_x/c-Si interface is treated as recombination sink, but it can also hold a charge that influences the band-bending, as known from detailed metal-insulator-semiconductor modeling [30]. This defect density $D_{it,cSi}$, the oxide thickness d_{ox}, the doping density $N_{D,\ poly}$ in the poly-Si layer and the peak dopant concentration $N_{D,cSi}$ in c-Si have been used to consistently describe the surface recombination and tunneling currents of electron- and hole-collecting poly-Si/SiO_x/c-Si junctions [29,31].

Here we use the MarcoPOLO model and its fast computational speed to deduce $D_{it,cSi}$ from lifetime measurements. We calculate the recombination parameter J_{0s} at the peak of the diffusion profile from the peak dopant concentration and the defect density $D_{it,cSi}$ at the SiO_x/c-Si interface. In addition to this surface recombination expressed by J_{0s}, Auger recombination is present within the diffusion profile. We calculate the sum of both recombination paths with the simulation software EDNA2 [32]. Therefore, we use the computed surface recombination parameter J_{0s} from the MarcoPOLO model as input and use the measured ECV profiles to calculate Auger recombination.

For this calculation, we assume that a) the defect density is the only interface charge in the junction, b) recombination at places where the oxide is broken up locally (pinholes) [33,34] is negligible, and c) recombination over point defects in the diffusion profiles is negligible. With these assumptions, the only recombination path is over defect states at SiO_x/c-Si interface, and the resulting $D_{it,cSi}$ values mark the upper limit for the actual defect density. We use a capture-cross-section of holes of $4.2 \times 10^{-18}\text{cm}^2$ which leads to the same results as the energy-dependent hole capture-cross-sections reported by Aberle et al. [35].

We perform a Monte-Carlo analysis with 500 samples per measure-

ment in which we vary the oxide thickness as $d_{ox} = (1.5 \pm 0.2)$ nm, the poly-Si doping concentration as $N_{D,poly} = (3.0 \pm 0.1) \times 10^{20} cm^{-3}$ and the c-Si peak doping concentration as $N_{D,cSi} = (1.4 \pm 0.5) \times 10^{19} cm^{-3}$ for the samples annealed at 820 °C and $N_{D,cSi} = (4.4 \pm 1.0) \times 10^{19} cm^{-3}$ for the samples annealed at 860 °C. The measured J_0 values are varied in the range of their standard deviation after multiple measurements on the same sample in the case of the 820 °C annealed samples or with a constant uncertainty range of 20% in the case of the 860 °C annealed samples. The resulting mean defect density and standard deviation of the obtained $D_{it,cSi}$ values after this analysis are shown as symbols and bars in Figs. 2, 3b and 6b.

3. Experimental results and discussion

a. Firing without hydrogen-containing capping layers:

As the hydrogen passivates the dangling bonds at the oxide interface, it is first of all interesting to know at what level the defect density is after annealing and how it develops qualitatively and quantitatively during firing. Since these values are not measurable by *C–V* measurements due to high leakage currents through the thin oxide, we calculate the mid-bandgap $D_{it,cSi}$ values for the POLO samples from our measured J_0 values using the MarcoPOLO model [29]. The results are shown in Fig. 2.

Before firing, which means, in this case, after annealing and without AlO_x or SiN_y capping layers, the interface state density is about ~2 × 10^{12} cm^{-2} eV^{-1}. Compared to samples having thermal grown interfacial oxides with a thickness of 10 nm showing $D_{it,cSi}$ values of about 1 × 10^{11} cm^{-2} eV^{-1}, determined by *C–V* measurements [20], these results are at least one order of magnitude higher. However, this agrees with the values reported for such thin oxides [29,36]. Here, the strong dopant diffusion into the wafer occurring in these samples, as opposed to samples with thicker oxides, provides for field-effect passivation so that despite the higher $D_{it,c\text{-}Si}$, the J_0 values are very low.

Firing then results in a substantial increase in $D_{it,cSi}$ to about 3–7 × 10^{12} cm^{-2} eV^{-1}, showing an approx. exponential dependence between the $D_{it,cSi}$, and the measured firing temperature. This trend fits the results recently shown on samples with a 10 nm-thick thermally grown

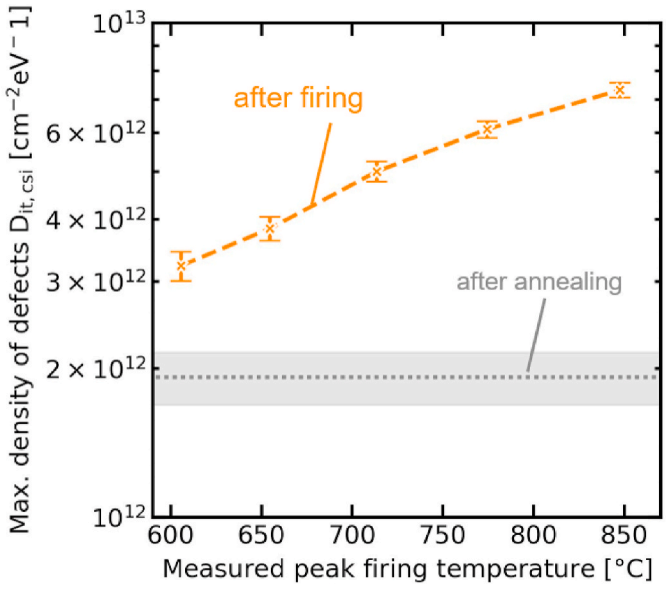

Fig. 2. Maximum interface defect density as a function of the measured firing peak temperature. The samples were annealed at 860 °C and fired without a capping layer. Orange data points are measured after firing. The grey interval depicts the results directly after annealing measured on all samples from the batch (upper/lower quartile). (For interpretation of the references to color in this figure legend, the reader is referred to the Web version of this article.)

interfacial oxide, but otherwise identical samples, using $D_{it,cSi}$ values determined by *C–V* measurements [20,36]. We fit the data from Fig. 2 with an Arrhenius law and obtain an activation energy of 0.29 ± 0.01 eV, which agrees very well with the obtained value of 0.30 ± 0.03 eV on the thicker thermal oxide [20]. This result indicates an underlying thermally activated process which is possibly similar for the two oxides.

b. Firing with an AlO_x/SiN_y stack (at 724 °C)

To determine the influence of an AlO_x layer on the hydrogen concentration, the J_0, and the defect state density at the poly-Si/SiO_x/c-Si interface, we prepare different test samples with varying AlO_x layer thicknesses between 2 and 15 nm.

Fig. 3 shows samples fired at a lower measured peak temperature of 724 °C, for which no blistering is expected from previous experiments and not found in optical microscope images. Here it can be seen that the J_0 values achieved after annealing of about 6 fA/cm^2 can be further improved to below 4 fA/cm^2 by depositing the two dielectric layers (AlO_x/SiN_y). The $D_{it,cSi}$ values after annealing are approx. 3.6 × 10^{12} cm^{-2} eV^{-1} and thus higher than in the samples in Fig. 2, processed in an earlier batch. One difference between those batches is the higher annealing temperature of 860 °C for the samples in Fig. 2. In contrast to that, the samples in Fig. 3 were annealed at 820 °C. A possible explanation for this difference could be that annealing at 860 °C yields a stronger re-arrangement of the bonds at the c-Si/SiO_x interface. This process, which is also responsible for the pinhole formation, could positively affect the $D_{it,c\text{-}Si}$. Furthermore, this would fit the argument that film tension plays a role since these should be reduced locally during pinhole formation.

In the state after the AlO_x and SiN_y depositions and before firing, a slight trend of decreasing J_0 with increasing AlO_x layer thickness can be seen. However, due to the comparatively small changes and the large error bars, we cannot exclude that this trend is due to process variations during SiN_y deposition. The subsequent firing has hardly any influence on the J_0 and $D_{it,cSi}$ values, and thus, before and after firing, we achieve excellent J_0 values. The samples with a 15 nm thick AlO_x layer show particularly good values below 2 fA/cm^2.

As we quantified the SIMS profiles shown in Figs. 4, 5 and 7 using implanted Si standards, the calculated values only apply to the poly-Si and c-Si layers and not to the SiN_y layers. However, the hydrogen concentration inside an unfired SiN_y layer was determined by FTIR measurements yielding a concentration of 6 × 10^{21} cm^{-3}. Comparing the uncalibrated values inside the SiN_y layer in Figs. 4, 5 and 7, we see no measurable loss of hydrogen between the states “before” and “after firing”.

The peak hydrogen concentration at the SiO_x/c-Si interface after firing at 725 °C in Fig. 5, which is in the range of 1–3.5 × 10^{18} cm^{-3} and the deuterium concentration in the range of 1.5 × 10^{17} cm^{-3} down to the detection limit of about 1 × 10^{16} cm^{-3} are more than three magnitudes lower than the actually determined hydrogen concentration of 6 × 10^{21} cm^{-3} inside the SiN_y layer. These peak concentrations are moreover showing an increasing trend with increasing AlO_x layer thickness. However, the fact that the hydrogen concentration increases with AlO_x layer thickness does not fit the expectation of the hydrogen blocking property of aluminum oxide mentioned above. A possible explanation could be that the AlO_x layer itself contributes a significant amount of hydrogen to the hydrogen in-diffusion. In fact, what is puzzling is that the deuterium concentration also increases at the same time. Since deuterium-containing gas (D_2) was only used for the SiN_y deposition, the deuterium cannot originate from the AlO_x layer and thus must have diffused through it. Another possibility would be an incorporation of D into the AlO_x layer during SiN_y deposition, in which case, however, we would not expect any increase of D with increasing thickness of the AlO_x layer. Therefore, the increased D concentration at the c-Si interface with increasing AlO_x thickness and the discrepancy to previous findings on H diffusion through Al_2O_3 [22] needs further investigation. A possible

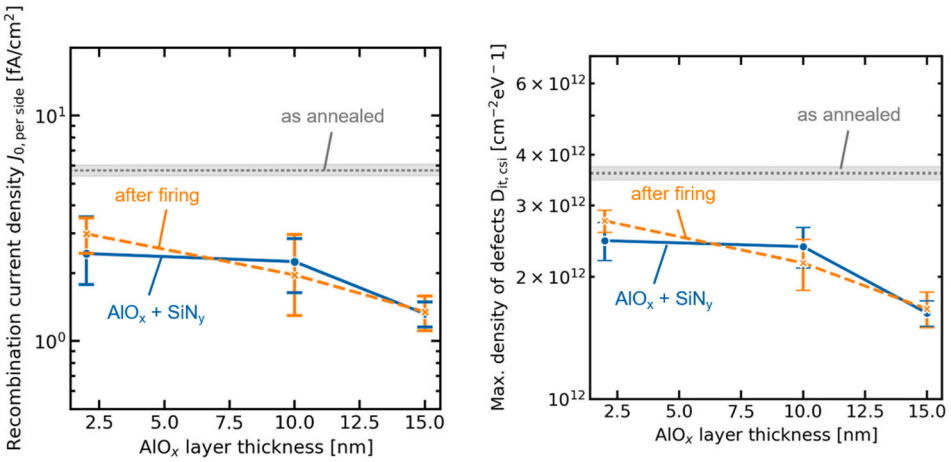

Fig. 3. a) Recombination current density and b) maximum defect state density of samples capped with AlO_x/SiN_y stacks, fired at 724 °C and varying AlO_x layer thickness measured before and after firing. The grey interval depicts the results directly after annealing at 820 °C measured on all samples from that batch. Blue data points are measured before firing, after the AlO_x and SiN_y deposition, and orange data points are measured after firing. (For interpretation of the references to color in this figure legend, the reader is referred to the Web version of this article.)

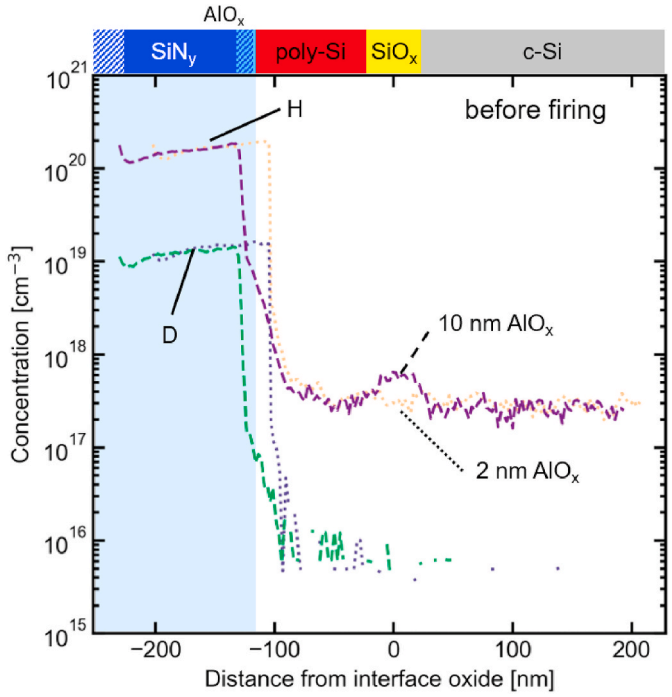

Fig. 4. Hydrogen and deuterium ToF-SIMS profiles in unfired n-type poly-Si/SiO_x contacts for different AlO_x layer thickness. The concentrations are only valid for the silicon parts of the sample and are not calibrated within the blue-marked SiN_y and AlO_x regions. (For interpretation of the references to color in this figure legend, the reader is referred to the Web version of this article.)

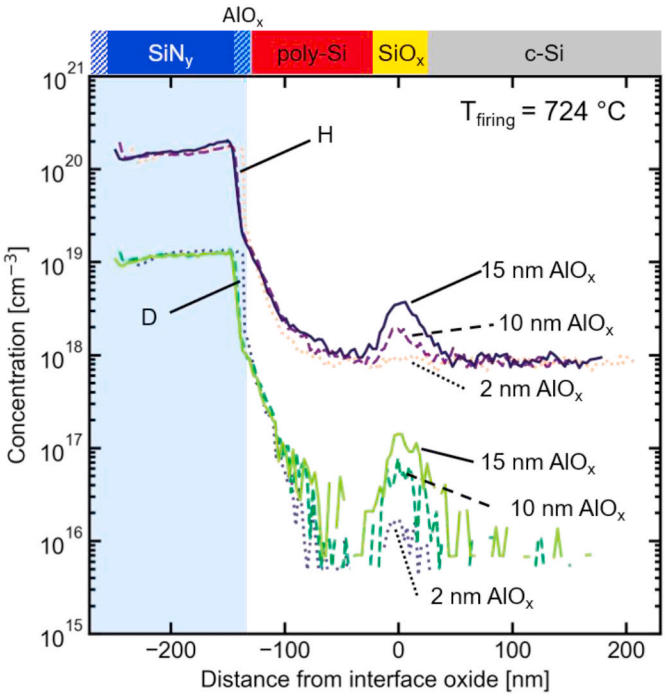

Fig. 5. Hydrogen and deuterium ToF-SIMS profiles in fired (T_{firing} = 724 °C) n-type poly-Si/SiO_x contacts as a function of the AlO_x layer thickness. The concentrations are only valid for the silicon parts of the sample and are not calibrated within the blue-marked SiN_y and AlO_x regions. (For interpretation of the references to color in this figure legend, the reader is referred to the Web version of this article.)

explanation might involve D-H exchange reactions, as suggested in Ref. [37].

Overall, these results indicate that there could be a positive influence of an increasing concentration of hydrogen in the range of 1–3.5 × 10^{18} cm^{-3} on the passivation of the poly-Si/SiO_x/c-Si interface states and J_0 values. At the low firing temperature of 724 °C used here, the active defect density is reduced with increasing hydrogen content at the poly-Si/SiO_x/c-Si interface. However, this trend can already be seen from the J_0 values directly after deposition of the dielectric layers, i.e., before firing. Fig. 4, which shows the hydrogen concentration of two samples before firing, shows that the samples with the thicker AlO_x layer (10 nm) have slightly more hydrogen at the poly-Si/SiO_x/c-Si interface even before firing compare to the sample with 2 nm AlO_x. As the temperature in the deposition chamber during SiN_y deposition is 500 °C, an in-diffusion of H from the AlO_x layers is likely. The deuterium concentrations of both samples inside the poly-Si, SiO_x, and poly-Si are below the resolution limit. This suggests that H from the AlO_x layer accumulates at the interface even before firing due to the high T of the nitride deposition. The present defects are probably already passivated during this initial hydrogenation of the oxide interfaces (with H from AlO_x). Upon firing, additional H and D is released from the nitride, as evidenced by the deuterium peaks in Fig. 5. The newly released D could exchange with H at the already passivated defects [37], causing higher D peaks for thicker AlO_x layers (see Fig. 5).

c. Firing with an AlO_x/SiN_y stack (at 863 °C)

Fig. 6 shows the J_0 and $D_{it,cSi}$ values of samples before and after firing at 863 °C. At this temperature, samples with just SiN_y layers showed a

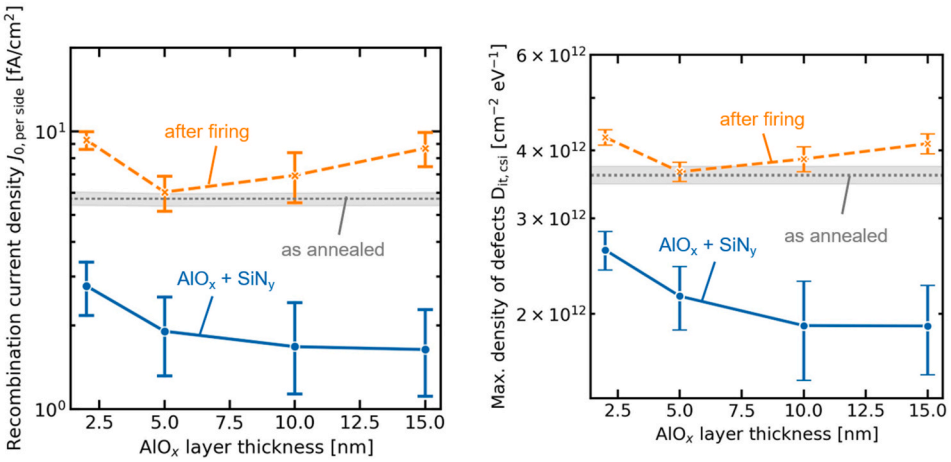

Fig. 6. a) Recombination current density and b) interface defect density of samples capped with AlO_x/SiN_y stacks, fired at 863 °C and varying AlO_x layer thickness measured before and after firing. The grey interval depicts the results directly after annealing at 820 °C measured on all samples from that batch. Blue data points are measured before firing, after the AlO_x and SiN_y deposition, and orange data points are measured after firing. (For interpretation of the references to color in this figure legend, the reader is referred to the Web version of this article.)

strong deterioration of the J_0 up to 20 fA/cm^2, as shown before [20]. After firing at 863 °C, all samples with a stack of AlO_x and SiN_y layers experience a deterioration of the passivation quality, as the J_0 values increase to over 6 fA/cm^2 and the defect density increases to 3.6 to 4.2 × 10^{12} cm^{-2} eV^{-1}. The passivation quality shows a slight optimum at an AlO_x film thickness of 5 nm. Again, the trends should be treated with caution compared to the scattering of the data. Furthermore, it is important to note that the sample with the thickest AlO_x layer of 15 nm-thickness shows homogeneous blistering.

Fig. 7 shows the ToF-SIMS measurements after firing at 863 °C. When looking at the H and D concentrations at the interface, it can be seen that the sample with 5 nm AlO_x has the highest H peak concentrations of 5.2 × 10^{18} cm^{-3}. The samples with 10 and 15 nm AlO_x show values of 3.4 × 10^{16} cm^{-3} which are only slightly below this, whereas the sample with 15 nm AlO_x shows a clearly broader peak and thus has more H and D stored in the area around the boundary surface. The sample with the smallest AlO_x thickness of 2 nm again shows the lowest peak H and D concentration (H: 1 × 10^{18} cm^{-3}, D: 8 × 10^{16} cm^{-3}) at the SiO_x/c-Si interface. Compared to the samples fired at 725 °C (see Fig. 5), the samples with 10 nm and 15 nm AlO_x show a slight increase in peak concentration, and also the sample with 5 nm AlO_x shows a higher peak concentration than the samples fired at 725 °C with 2 and 10 nm (a directly comparable sample with 5 nm AlO_x is not present in this group).

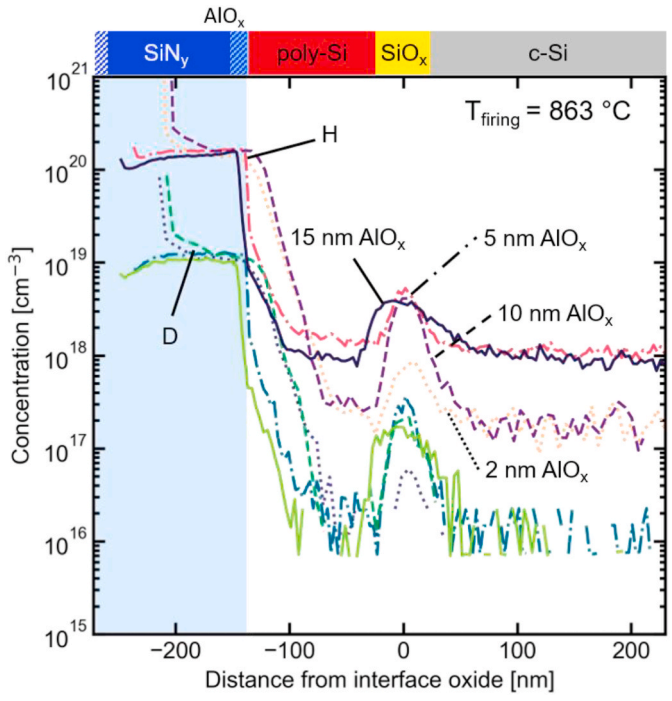

Fig. 7. Hydrogen and deuterium ToF-SIMS profiles in fired (T_{firing} = 863 °C) n-type poly-Si/SiO_x contacts as a function of the AlO_x layer thickness. The concentrations are only valid for the silicon parts of the sample and are not calibrated within the blue-marked SiN_y and AlO_x regions. (For interpretation of the references to color in this figure legend, the reader is referred to the Web version of this article.)

Now considering the hydrogen concentration in the poly-Si regions, it turns out that the two samples with 2 nm and 10 nm AlO_x show concentrations that are about one order of magnitude lower than in all the other fired samples. A possible explanation could be that the H background level during the measurement of those two samples was particularly low, while a higher H background level influenced the measured values of the other samples during their measurements. However, all the samples were measured a second time, and the same results were obtained. Thus, an explanation of the different H concentrations in the poly-Si is pending so far.

As already seen with the samples fired at 725 °C, the samples fired at 863 °C also do not show a decreasing trend of the hydrogen and deuterium concentration at the interface with increasing AlO_x layer thickness.

d. Comparison of integrated hydrogen concentrations and defect state densities at the interface:

Fig. 8 shows the integrated hydrogen concentrations over the peaks in the SiO_x/c-Si interface region for all measured samples. This allows a comparison of the data from the different samples. Here it can be seen once again that the hydrogen concentration at the SiO_x/c-Si interface increases significantly as a result of firing. The concentrations after firing for the samples with 10 nm and 15 nm AlO_x show an increasing trend with increasing firing temperature. However, for the samples with a 2 nm thick layer, the sample fired at 724 °C has significantly more hydrogen at the interface.

Under the simplifying assumption of a constant defect distribution across the bandgap, we calculate an aerial defect density by multiplying the $D_{it,c\text{-}Si}$ values with the bandgap energy of 1.2 eV indicated by the colored intervals. Fig. 8 thus allows a rough comparison between the hydrogen and the defect density at the interface. After the annealing at 820 °C, the defect concentration is about 4–5 × 10^{12} cm^{-2}, which is reduced to 2–3 × 10^{12} cm^{-2} by the induced hydrogen concentration of 3 × 10^{12} cm^{-2}. After firing, the hydrogen concentrations are, according to this rough estimation, for the most part, several times above the measured defect densities of these samples fired with hydrogen-containing capping layers. Moreover, the H concentrations also exceed

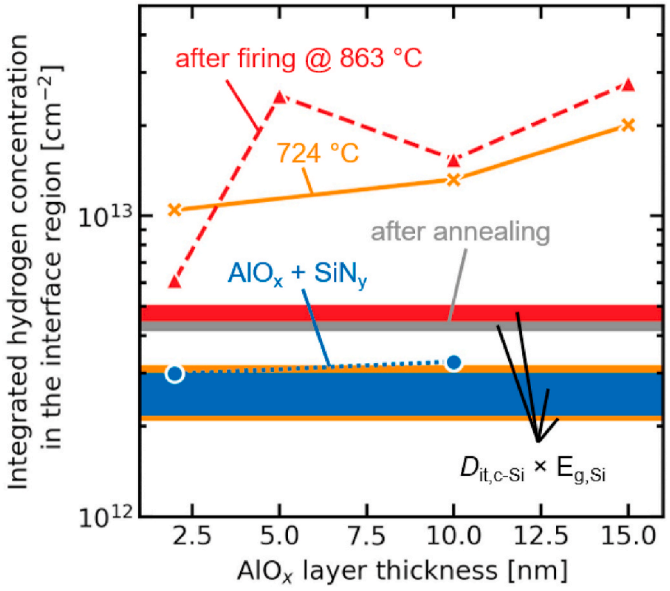

Fig. 8. Integrated hydrogen concentrations over the peak in the SiOx/c-Si interface as a function of the AlO_x layer thickness. Blue data points are measured after annealing, orange data points are measured after firing at 724 °C, and red data points are measured after firing at 863 °C. The intervals indicate the intervals of $D_{it,c\text{-}Si} \times E_{g,Si}$ values determined under the assumption of a constant $D_{it,c\text{-}Si}$ distribution over the bandgap (e.g. the $D_{it,c\text{-}Si}$ is multiplied by 1.2 eV to get an aerial concentration). The colors of the intervals show analogously to the data points the state for which the respective values were determined. (For interpretation of the references to color in this figure legend, the reader is referred to the Web version of this article.)

the defect concentration of samples fired without hydrogen-containing layers (shown in Fig. 2), in which no defects are rendered "invisible" by hydrogen passivation. Despite the apparent oversupply of H, however, the defect density increases during firing at 863 °C. This behavior supports our hypothesis that the excessive hydrogenation of the interface during firing, on the one hand, passivates defects induced by the firing process but, on the other hand, also creates additional defects, which, however, remain hydrogenated and passivated at lower firing temperatures. Such additional defects, like platelets, could explain the high concentrations of H at the interface.

With rising thermal activation by a higher firing temperature, the delicate balance between new defects and hydrogenation likely shifts to more active defects. Our latest paper [20] raised the hypothesis that thermal stress at the SiO_x/c-Si interface plays a role during firing. The suggestion we made is thermal stress induced by the mismatch in thermal expansion coefficients between the poly-Si and the SiO_x [38], which increases with increasing temperature, facilitates defect formation. The in-diffusing hydrogen then likely inserts into these weakened, strained bonds or dangling interface bonds, which could lead to the formation and growth of platelets [21,39–42]. These are well known to trigger the formation of blisters, especially from hydrogen implanted c-Si and poly-Si [43], which we also see in this experiment on the samples with 15 nm AlO_x.

As seen in Fig. 8 again, this experiment does not indicate a hydrogen-blocking property of the AlO_x layers that increases with increasing AlO_x layer thickness, which was seen by Helmich et al. [22]. However, compared to their experiments where they used SiN_y layers with a refractive index of 2.3 and an approximate hydrogen content of more than 15% [44], in these experiments, we used SiN_y layers with a refractive index of 2.05 and thus a significantly lower hydrogen content of 5.5%. Moreover, the ratio of the hydrogen-containing species i.e. Si–H and N–H, change with the refractive index and are therefore different in both experiments [44]. It is also known that Si–H and N–H have different activation energy for the release of hydrogen [45], and also the blocking behavior of AlO_x for these species could be different. Moreover, the high T of the nitride deposition used in this experiment and the thus induced H in-diffusion during this process could also be a reason for the observed differences.

4. Conclusion

In conclusion, we determined the density of defect states of nPOLO junctions featuring a wet chemical interfacial oxide from lifetime measurements using the MarcoPOLO model before firing. In samples that did not receive any hydrogen treatment, the $D_{it,cSi}$ is about 2×10^{12} cm^{-2} eV^{-1} and rises to 3–7 $\times$ 10^{12} cm^{-2} eV^{-1} during firing at measured peak temperatures between 620 °C and 863 °C.

Applying a stack of hydrogen-containing AlO_x and SiN_y layers, we could confirm that the hydrogen concentration at the oxide interface of poly-Si samples increases significantly during firing. At the same time, we did not see a decreasing trend with increasing AlO_x thickness.

From a rough comparison of the hydrogen concentrations and the defect densities after annealing and AlO_x and SiN_y depositon, it can be said that they are in the same order of magnitude. However, after firing, the hydrogen concentration exceeds the defect concentration several times, indicating that the hydrogen is also stored in other places than former dangling bonds, which we speculate are hydrogen-induced, newly created defects. For a more detailed understanding of the effects and to be able to distinguish between the different simultaneous defect formation and passivation processes, further investigations are necessary.

From an application point of view, these and the former results [20] indicate that using an AlO_x/SiN_y stack rather than a single SiN_y capping layer can bring an advantage for the passivation quality after firing. However, if one considers the entire cell process, it should be noted that an adaptation of the subsequent processes is necessary, e.g., the choice of a different Ag paste than used for SiN_y alone [46].

CRediT authorship contribution statement

Christina Hollemann: Writing – original draft, Visualization, Investigation, Conceptualization. **Nils Folchert:** Methodology, Conceptualization, Investigation, Writing – review & editing. **Steven P. Harvey:** Investigation, Writing – review & editing. **Paul Stradins:** Conceptualization, Methodology, Writing – review & editing. **David L. Young:** Conceptualization, Writing – review & editing. **Caroline Lima Salles de Souza:** Conceptualization, Writing – review & editing. **Michael Rienäcker:** Conceptualization, Writing – review & editing. **Felix Haase:** Conceptualization, Writing – review & editing. **Rolf Brendel:** Funding acquisition, Supervision, Writing – review & editing. **Robby Peibst:** Conceptualization, Supervision, Project administration, Funding acquisition, Writing – review & editing.

Declaration of competing interest

The authors declare that they have no known competing financial interests or personal relationships that could have appeared to influence the work reported in this paper.

Acknowledgments

The authors thank the Federal Ministry for Economic Affairs and Energy (BMWi) and the state of Lower Saxony for funding this work, Hilke Fischer, Annika Raugewitz, Anja Christ (all from ISFH), Raymond Zieseniss and Guido Glowatzki (both from the Institute of Electronic Materials and Devices) for sample processing and Martin Rudolf and Henning Schulte-Huxel for the FTIR measurement. This work was authored in part by the National Renewable Energy Laboratory, operated by Alliance for Sustainable Energy, LLC, for the U.S. Department of

Energy (DOE) under Contract No. DE-AC36-08GO28308. Funding provided by the U.S. Department of Energy Office of Energy Efficiency and Renewable Energy Solar Energy Technologies Office. The views expressed in the article do not necessarily represent the views of the DOE or the U.S. Government. The U.S. Government retains and the publisher, by accepting the article for publication, acknowledges that the U.S. Government retains a nonexclusive, paid-up, irrevocable, worldwide license to publish or reproduce the published form of this work, or allow others to do so, for U.S. Government purposes.

References

[1] A. Richter, R. Müller, J. Benick, F. Feldmann, B. Steinhauser, C. Reichel, A. Fell, M. Bivour, M. Hermle, S.W. Glunz, Design rules for high-efficiency both-sides-contacted silicon solar cells with balanced charge carrier transport and recombination losses, Nat. Energy 6 (2021) 429–438, https://doi.org/10.1038/s41560-021-00805-w.

[2] F. Haase, C. Hollemann, S. Schäfer, A. Merkle, M. Rienäcker, J. Krügener, R. Brendel, R. Peibst, Laser contact openings for local poly-Si-metal contacts enabling 26.1%-efficient POLO-IBC solar cells, Sol. Energy Mater. Sol. Cell. 186 (2018) 184–193, https://doi.org/10.1016/j.solmat.2018.06.020.

[3] International Technology Roadmap for Photovoltaics, ITRPV), 2021.

[4] JinkoSolar Co. Ltd, JinkoSolar has n-type mono cell verified at record 24.79% conversion efficiency. https://www.pv-tech.org/jinkosolar-has-n-type-mono-cell-verified-at-record-24.79-conversion-efficie/, 2020. (Accessed 7 May 2021).

[5] A. Mewe, M. Stodolny, J. Anker, M. Lenes, X. Pagès, Y. Wu, K. Tool, B. Geerligs, I. Romijn, Full Wafer Size IBC Cell with Polysilicon Passivating Contacts. Proceeding of the SiliconPV 2018, AIP Publishing, Lausanne, Switzerland, 2018, p. 40014.

[6] H.E. Çiftpınar, M.K. Stodolny, Y. Wu, G.J. Janssen, J. Löffler, J. Schmitz, M. Lenes, J.-M. Luchies, L.J. Geerligs, Study of screen printed metallization for polysilicon based passivating contacts, Energy Procedia 124 (2017) 851–861, https://doi.org/10.1016/j.egypro.2017.09.242.

[7] M.K. Stodolny, M. Lenes, Y. Wu, G. Janssen, I.G. Romijn, J. Luchies, L.J. Geerligs, n-Type polysilicon passivating contact for industrial bifacial n-type solar cells, Sol. Energy Mater. Sol. Cell. 158 (2016) 24–28, https://doi.org/10.1016/j.solmat.2016.06.034.

[8] D. Kang, H.C. Sio, D. Yan, J. Stuckelberger, R. Liu, D. Macdonald, Firing stability of doped polysilicon passivation layers. 5 pages/37th European photovoltaic solar energy conference and exhibition; 188-192, in: in: Proc. 37th European Photovoltaic Solar Energy Conf., Sept. 2020, WIP Munich, 2020 online.

[9] B.W. van de Loo, B. Macco, M. Schnabel, M.K. Stodolny, A.A. Mewe, D.L. Young, W. Nemeth, P. Stradins, W.M. Kessels, On the hydrogenation of Poly-Si passivating contacts by Al2O3 and SiN thin films, Sol. Energy Mater. Sol. Cell. 215 (2020) 110592, https://doi.org/10.1016/j.solmat.2020.110592.

[10] B. Nemeth, D.L. Young, M.R. Page, V. LaSalvia, S. Johnston, R. Reedy, P. Stradins, Polycrystalline silicon passivated tunneling contacts for high efficiency silicon solar cells, J. Mater. Res. 31 (2016) 671–681, https://doi.org/10.1557/jmr.2016.77.

[11] G. Yang, A. Ingenito, N. van Hameren, O. Isabella, M. Zeman, Design and application of ion-implanted polySi passivating contacts for interdigitated back contact c-Si solar cells, Appl. Phys. Lett. 108 (2016) 33903, https://doi.org/10.1063/1.4940364.

[12] Y. Yang, P.P. Altermatt, Y. Cui, Y. Hu, D. Chen, L. Chen, G. Xu, X. Zhang, Y. Chen, P. Hamer, R.S. Bonilla, Z. Feng, P.J. Verlinden, Effect of Carrier-Induced Hydrogenation on the Passivation of the Poly-Si/SiOx/c-Si Interface, Author(s), Lausanne, Switzerland, 2018, p. 40026.

[13] A. Ingenito, G. Nogay, Q. Jeangros, E. Rucavado, C. Allebé, S. Eswara, N. Valle, T. Wirtz, J. Horzel, T. Koida, M. Morales-Masis, M. Despeisse, F.-J. Haug, P. Löper, C. Ballif, A passivating contact for silicon solar cells formed during a single firing thermal annealing, Nat. Energy 3 (2018) 800–808, https://doi.org/10.1038/s41560-018-0239-4.

[14] H.E. Çiftpınar, M.K. Stodolny, Y. Wu, G.J. Janssen, J. Löffler, J. Schmitz, M. Lenes, J.-M. Luchies, L.J. Geerligs, Study of screen printed metallization for polysilicon based passivating contacts, Energy Procedia 124 (2017) 851–861, https://doi.org/10.1016/j.egypro.2017.09.242.

[15] S. Duttagupta, N. Nandakumar, P. Padhamnath, J.K. Buatis, R. Stangl, A.G. Aberle, monoPoly™ cells: large-area crystalline silicon solar cells with fire-through screen printed contact to doped polysilicon surfaces, Sol. Energy Mater. Sol. Cell. 187 (2018) 76–81, https://doi.org/10.1016/j.solmat.2018.05.059.

[16] Z. Rui, Y. Zeng, X. Guo, Q. Yang, Z. Wang, C. Shou, W. Ding, J. Yang, X. Zhang, Q. Wang, H. Jin, M. Liao, S. Huang, B. Yan, J. Ye, On the passivation mechanism of poly-silicon and thin silicon oxide on crystal silicon wafers, Sol. Energy 194 (2019) 18–26, https://doi.org/10.1016/j.solener.2019.10.064.

[17] B. Steinhauser, F. Feldmann, D. Ourinson, H. Nagel, T. Fellmeth, M. Hermle, On the influence of the SiN x composition on the firing stability of poly-Si/SiN x stacks, Phys. Stat. Sol. 217 (2020), 2000333, https://doi.org/10.1002/pssa.202000333.

[18] F. Feldmann, M. Bivour, C. Reichel, M. Hermle, S.W. Glunz, Passivated rear contacts for high-efficiency n-type Si solar cells providing high interface passivation quality and excellent transport characteristics, Sol. Energy Mater. Sol. Cell. 120 (2014) 270–274, https://doi.org/10.1016/j.solmat.2013.09.017.

[19] M. Lehmann, N. Valle, J. Horzel, A. Pshenova, P. Wyss, M. Döbeli, M. Despeisse, S. Eswara, T. Wirtz, Q. Jeangros, A. Hessler-Wyser, F.-J. Haug, A. Ingenito, C. Ballif, Analysis of hydrogen distribution and migration in fired passivating contacts (FPC), Sol. Energy Mater. Sol. Cell. 200 (2019) 110018. https://doi.org/10.1016/j.solmat.2019.110018.

[20] C. Hollemann, M. Rienäcker, A. Soeriyadi, C. Madumelu, F. Haase, J. Krügener, B. Hallam, R. Brendel, R. Peibst, Firing stability of tube furnace-annealed n-type poly-Si on oxide junctions, Prog. Photovoltaics Res. Appl. accepted for publication.

[21] N. Johnson, F. Ponce, R. Street, R. Nemanich, Defects in single-crystal silicon induced by hydrogenation, Phys. Rev. B 35 (1987) 4166–4169, https://doi.org/10.1103/physrevb.35.4166.

[22] L. Helmich, D.C. Walter, D. Bredemeier, J. Schmidt, Atomic-layer-deposited Al 2 O 3 as effective barrier against the diffusion of hydrogen from SiN x :H layers into crystalline silicon during rapid thermal annealing, Phys. Status Solidi RRL 96 (2020) 2000367, https://doi.org/10.1002/pssr.202000367.

[23] J.-I. Polzin, F. Feldmann, B. Steinhauser, M. Hermle, S.W. Glunz, Study on the interfacial oxide in passivating contacts, in: 15th International Conference on Concentrator Photovoltaic Systems (CPV-15), Fes, Morocco, AIP Publishing, 2019, p. 40016.

[24] D. Tetzlaff, J. Krügener, Y. Larionova, S. Reiter, M. Turcu, F. Haase, R. Brendel, R. Peibst, U. Höhne, J.-D. Kähler, T. Wietler, A simple method for pinhole detection in carrier selective polo-junctions for high efficiency silicon solar cells, Solar Energy Mater. Solar Cells (2017), https://doi.org/10.1016/j.solmat.2017.05.041.

[25] F.A. Stevie, C. Zhou, M. Hopstaken, M. Saccomanno, Z. Zhang, A. Turansky, SIMS measurement of hydrogen and deuterium detection limits in silicon: comparison of different SIMS instrumentation, J. Vac. Sci. Technol. Nanotechnol. Microelectron. 34 (2016), 03H103, https://doi.org/10.1116/1.4940151.

[26] D.E. Kane, R.M. Swanson, Measurement of the emitter saturation current by a contactless photoconductivity decay method, in: 18th IEEE Photovoltaic Specialists Conference, IEEE, 1985, pp. 578–583.

[27] A. Richter, F. Werner, A. Cuevas, J. Schmidt, S. Glunz, Improved parameterization of auger recombination in silicon, Energy Procedia 27 (2012) 88–94, https://doi.org/10.1016/j.egypro.2012.07.034.

[28] Z. Yin, F.W. Smith, Optical dielectric function and infrared absorption of hydrogenated amorphous silicon nitride films: Experimental results and effective-medium-approximation analysis, Physical Review B 42 (1990) 3666–3675. https://doi.org/10.1103/physrevb.42.3666.

[29] N. Folchert, R. Peibst, R. Brendel, Modeling recombination and contact resistance of poly-Si junctions, Prog. Photovoltaics Res. Appl. 28 (2020) 1289–1307, https://doi.org/10.1002/pip.3327.

[30] R. Girisch, R.P. Mertens, R.F. de Keersmaecker, Determination of Si-SiO/sub 2/ interface recombination parameters using a gate-controlled point-junction diode under illumination, IEEE Trans. Electron. Dev. 35 (1988) 203–222, https://doi.org/10.1109/16.2441.

[31] N. Folchert, S. Bordihn, R. Peibst, R. Brendel, Modelling the annealing of poly-Si/SiOx/c-Si junctions, Energy Procedia (2021). Submitted for publication.

[32] K.R. McIntosh, P.P. Altermatt, A freeware 1D Emitter model for silicon solar cells, in: 35th IEEE Photovoltaic Specialists, 2010, pp. 2188–2193.

[33] R. Peibst, U. Römer, K.R. Hofmann, B. Lim, T.F. Wietler, J. Krugener, N.-P. Harder, R. Brendel, A simple model describing the symmetric I-V characteristics of p polycrystalline Si/n monocrystalline Si, and n polycrystalline Si/p monocrystalline junctions, IEEE J. Photovoltaics 4 (2014) 841–850, https://doi.org/10.1109/JPHOTOV.2014.2310740.

[34] R. Peibst, U. Römer, Y. Larionova, M. Rienäcker, A. Merkle, N. Folchert, S. Reiter, M. Turcu, B. Min, J. Krügener, D. Tetzlaff, E. Bugiel, T. Wietler, R. Brendel, Working principle of carrier selective poly-Si/c-Si junctions: is tunnelling the whole story? Sol. Energy Mater. Sol. Cell. 158 (2016) 60–67, https://doi.org/10.1016/j.solmat.2016.05.045.

[35] A.G. Aberle, S. Glunz, W. Warta, Impact of illumination level and oxide parameters on Shockley–Read–Hall recombination at the Si-SiO 2 interface, J. Appl. Phys. 71 (1992) 4422–4431, https://doi.org/10.1063/1.350782.

[36] E.H. Nicollian, J.R. Brews, MOS (Metal Oxide Semiconductor) Physics and Technology, Wiley, New York, 1982.

[37] M. Schnabel, B.W.H. van de Loo, W. Nemeth, B. Macco, P. Stradins, W.M. M. Kessels, D.L. Young, Hydrogen passivation of poly-Si/SiO x contacts for Si solar cells using Al 2 O 3 studied with deuterium, Appl. Phys. Lett. 112 (2018) 203901, https://doi.org/10.1063/1.5031118.

[38] S.M. Hu, Stress-related problems in silicon technology, J. Appl. Phys. 70 (1991) R53–R80, https://doi.org/10.1063/1.349282.

[39] N.H. Nickel, G.B. Anderson, J. Walker, Hydrogen-induced platelets in disordered silicon, Solid State Commun. 99 (1996) 427–431, https://doi.org/10.1016/0038-1098(96)00283-9.

[40] N.M. Johnson, C. Herring, C. Doland, J. Walker, G.B. Anderson, F.A. Ponce, Hydrogen-induced platelets in silicon: separation of nucleation and growth, Mater. Sci. Forum 83–87 (1992) 33–38. https://doi.org/10.4028/www.scientific.net/msf.83-87.33.

[41] N. Nickel, G. Anderson, N. Johnson, J. Walker, Nucleation mechanism of hydrogen-induced platelets in single crystal and polycrystalline silicon, Phys. B Condens. Matter 273–274 (1999) 212–215, https://doi.org/10.1016/S0921-4526(99)00452-4.

[42] N.M. Johnson, C. Doland, F. Ponce, J. Walker, G. Anderson, Hydrogen in crystalline semiconductors, Phys. B Condens. Matter 170 (1991) 3–20, https://doi.org/10.1016/0921-4526(91)90104-M.

[43] R.-S. Huang, C.-H. Cheng, J.C. Liu, M.K. Lee, C.T. Chen, Electrical measurements on ion-implanted LPCVD polycrystalline silicon films, Solid State Electron. 26 (1983) 657–665, https://doi.org/10.1016/0038-1101(83)90021-7.

[44] D. Bredemeier, D. Walter, J. Schmidt, Impact of silicon nitride film properties on hydrogen in-diffusion into crystalline silicon, in: Proc. 36th European Photovoltaic Solar Energy Conf., Sept. 2019, 2019. Marseille, France, Marseille, France.

[45] F.L. Martínez, A. del Prado, I. Mártil, G. González-Diaz, W. Bohne, W. Fuhs, J. Röhrich, B. Selle, I. Sieber, Molecular models and activation energies for bonding rearrangement in plasma-deposited a−SiNx:H dielectric thin films treated by rapid thermal annealing, Phys. Rev. B 63 (2001), https://doi.org/10.1103/PhysRevB.63.245320.

[46] D. Ourinson, T. Fellmeth, S. Tepner, T. Javaid, M. Dhamrin, C. Turney, G. Emanuel, S.W. Glunz, M. Pospischil, F. Clement, Optimization of Al fire-through contacts for AlO X –SiN X rear passivated bifacial p -PERC, IEEE J. Photovoltaics 10 (2020) 1523–1531, https://doi.org/10.1109/JPHOTOV.2020.2983006.